Nanoscale

PAPER

View Article Online
View Journal | View Issue

Cite this: *Nanoscale*, 2026, **18**, 1474

Cryo-optical setup for wide-field microscopy and spectroscopy of luminescent nanomaterials

Lorenzo Tallarini, [a] Gioele Lapo,[a] Marzo C. López Cerón, [b] Ivan G. Scheblykin [a] and Dmitry Baranov *[a]

Studying photoluminescence (PL) is essential for understanding and engineering light-emitting nanomaterials. Heterogeneous samples, such as thin films and microstructures, require characterization of the spatial distribution of PL intensity, spectra, lifetimes, and photon correlations at the microscale under variable temperatures. Here we describe a cryo-optical setup for micro-PL imaging, spectroscopy, lifetime, and photon bunching measurements that addresses this need. The system combines a home-built wide-field microscope with a commercial closed-loop helium cryostat, a spectrograph equipped with an sCMOS camera, and a Hanbury-Brown and Twiss interferometer (HBT-interferometer). Optical layout and components of the setup are described, and its performance is tested on samples of $CsPbBr_3$ nanocrystal superlattices. This work aims to demonstrate that it is feasible to develop an advanced microscopy and spectroscopy setup suitable for material scientists focused on developing novel materials, even if they initially lack extensive experience in advanced optical methods.

Received 29th September 2025,
Accepted 12th December 2025

DOI: 10.1039/d5nr04127a

rsc.li/nanoscale

Introduction

Growing interest in the optical properties and electronic structure of nanomaterials has driven the integration of PL microscopy into materials science.[1] This is motivated by the desire to move beyond ensemble-averaged measurements and investigate the spatial and spectral heterogeneity of PL at the diffraction limit and beyond. This concept is rooted in single-molecule spectroscopy, a well-established field in molecular photo-physics started at the end of the 1980s, which found later vast applications in fluorescence imaging and optical super-resolution in biology and medicine.[2–4] These methods, developed primarily for optical imaging in biology, from basic wide-field microscopy[5] to super-resolution methods,[6–8] are increasingly used in the study of heterogeneous optoelectronic materials, most recently in lead halide perovskite semiconductors.[9–12] Temperature-dependent steady-state PL spectra and PL lifetime measurements are now appearing routinely in the literature, accompanying syntheses and structural characterization of novel compositions and formulations of luminescent materials.

Parallel to these developments, the buzz of quantum technology has stimulated research on colloidal quantum dots as solid-state light sources for single-photon emission and lasing, among other functions.[13,14] Colloidal quantum dots have significantly broadened the expertise required in materials science research, motivating chemists to move beyond synthesis toward detailed spectroscopic characterizations.[15] This created a demand for methods, such as cryogenic PL microscopy and spectroscopy, typically used in solid-state physics and quantum optics,[16] to be applied to materials synthesized in the wet lab, such as colloids, thin films, and various microstructures. Access to specialized setups for studying quantum emitters often relies on collaborations, which can limit the throughput of screening the samples and the discovery of interesting properties. Recent advances in commercially available equipment, such as closed-cycle cryostats with optical access and user-friendly control interfaces, have made advanced low-temperature spectroscopy more accessible. This enables synthetic and materials-focused research groups to expand characterization capabilities in-house, bridging the gap between synthesis, structural analysis, and optoelectronic measurements. These developments have created an intersection between chemistry, physics, and biology, as new PL materials obtained by chemical synthesis are studied using microscopy techniques from the life sciences and quantum optical tools from physics.

One example that is particularly interesting to us is metal halide perovskite nanocrystals, characterized by their bright emission and unusual electronic structure.[17–19] The characterization of perovskite nanocrystals as single-photon emitters has become increasingly common.[20–25] Besides single par-

[a]*Division of Chemical Physics and NanoLund, Department of Chemistry, Lund University, P.O. Box 124, Lund, SE-221 00, Sweden.*
E-mail: dmitry.baranov@chemphys.lu.se
[b]*Division of Atomic Physics, Department of Physics, Lund University, P.O. Box 118, SE-221 00 Lund, Sweden*

ticles, their self-assembly into ordered microscopic structures (variously referred to as superlattices, supercrystals, or mesocrystals) and resulting collective phenomena such as superfluorescence[26,27] and superradiance,[28,29] are of high scientific interest. Investigations of these curious properties and correlation of their origin with the sample morphology require PL studies of individual microscopic objects at cryogenic temperatures. Thus, we describe the layout and implementation of a cryo-optical setup for PL microscopy and spectroscopy, suitable for studying questions like these and generally applicable to the characterization of emerging luminescent nanomaterials in the *ca.* 4–320 K temperature range. The setup is built around a commercial cryostat, spectrograph, and camera, incorporating an HBT-interferometer. It allows spatial resolution of steady-state photoluminescence, spectrum- and time-resolved photoluminescence and spectrum-resolved correlation measurements within a single cooling cycle. The performance of the setup is tested on a sample of 8 nm $CsPbBr_3$ perovskite nanocrystal superlattices, a dilute nanocrystal film, and a solution of Rhodamine.

Layout of the setup and implementation

The cryo-optical setup consists of four modules: (1) cryostat with a sample and a microscope objective, (2) microscope optical path, (3) spectrograph and camera for spectroscopy, imaging, and spectral selection, and (4) an HBT-interferometer for spectrally-resolved PL and photon correlation measurements. The scheme of the setup is illustrated in Fig. 1 with the principal components listed in Table 1, and the implementation is shown in Fig. 2. The microscope optical path, consisting of the excitation and detection parts, links the components of the setup and enables wide-field PL microscopy. While not yet implemented, the flexible layout of the setup permits integration of a white-light source and a color camera for imaging in either transmission or reflection modes, as illustrated in Fig. S1.

The conditions for constructing this setup were determined by the targeted size of the illumination spot on the sample, as well as practical limitations such as the available light source and space on the cryostat breadboard and the optical table. Neglecting light diffraction and using the thin lens approximation, the main equations describing the optical parameters for the excitation part of the setup from fiber to objective are:[30]

$$\frac{1}{f_{\mathrm{Obj}}+a}+\frac{1}{f_{\mathrm{Obj}}+b}=\frac{1}{f_{\mathrm{Obj}}}, \tag{1}$$

$$\tan\alpha=\frac{(f_{\mathrm{Obj}}+b)\cdot\tan\psi}{f_{\mathrm{Obj}}+a}=\frac{f_{\mathrm{Obj}}+b}{f_{\mathrm{Obj}}+a}\cdot\frac{d_{\mathrm{L1}}}{2f_{\mathrm{L1}}}, \tag{2}$$

$$d_{\mathrm{spot}}=2a\tan\alpha=d_{\mathrm{L1}}\cdot\frac{f_{\mathrm{Obj}}}{f_{\mathrm{L1}}}. \tag{3}$$

The variables are shown in Fig. 1. Briefly, eqn (1) is the lens equation for the objective (O), eqn (2) is a geometric relation between focusing angles of the objective (α) and L1 (ψ), and eqn (3) defines the diameter of the wide-field illumination spot on the sample (d_{spot}) as a function of the incident beam spot size on the L1 (d_{L1}) and focal distances of the objective (f_{Obj}) and L1 (f_{L1}). The final equality in the eqn (3) is obtained by solving eqn (1) for a or b (where a is the distance from image to the rear focal plane of the objective, b is the distance between f_{L1} and the front focal plane of the objective) and substituting it in eqn (2).

The light source was a 405 nm pulsed laser diode. Its output was coupled into the optical fiber at one end of the laboratory and then brought onto the cryostat breadboard

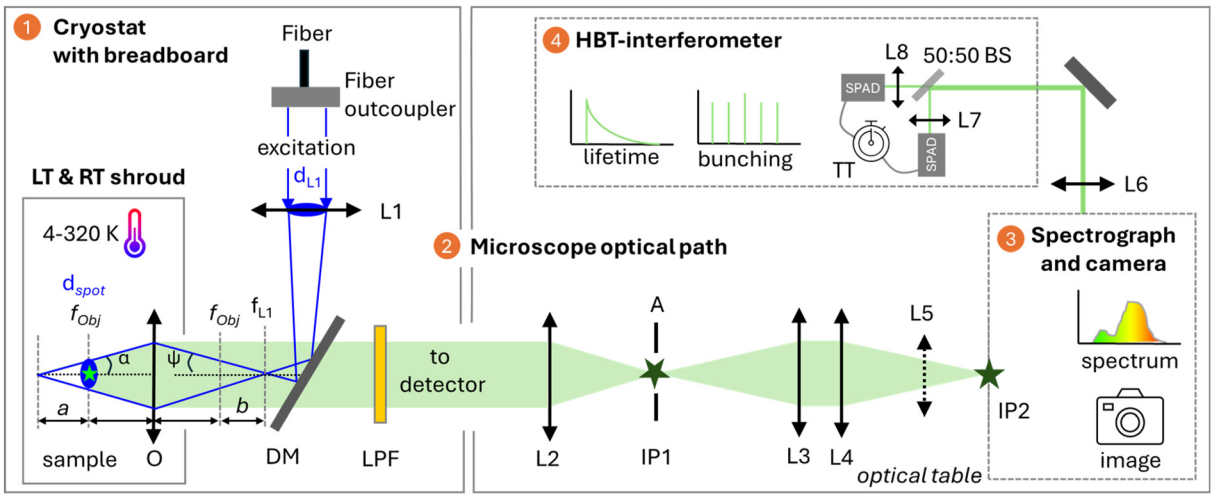

Fig. 1 Schematic of the cryo-optical setup with components indicated: (1) cryostat with a breadboard and a shroud hosting a sample and a low-temperature objective (O), (2) microscope optical path (IP – image plane), (3) spectrograph and camera for spectroscopy, imaging, and spectral selection, and (4) HBT-interferometer. For abbreviations of optical components and variables, see Table 1 and eqn (1)–(3), respectively.

Table 1 List of components used in the setup and their selected specifications. For complete specifications, please refer to the supplier using the provided part numbers

Component	Part (supplier)	Selected specifications
Excitation light source	LDH-D-C-405 (PicoQuant)	Pulsed diode laser, 405 nm, nominal minimum pulse width 49 ps
Fiber	SM300 (ThorLabs)	Single-mode, 320–430 nm, *ca.* 2.4 μm mode-field diameter at 350 nm, 4 m long
Fiber coupler	PAF2S-5A (ThorLabs)	f = 4.6 mm, 350–700 nm
Lens (L1)	LA4236-A (ThorLabs)	f = 125.4 mm, 1″ diam., uncoated, UV fused silica (UVFS), plano-convex lens
Dichroic mirror (DM)	DMLP425R (ThorLabs)	25 mm × 36 mm, 425 nm cut-on
Longpass filter (LPF)	FELH0425 (ThorLabs)	25.0 mm diam., 425 nm cut-on
Cryostat	attoDRY800xs (Attocube)	Closed-cycle helium cryostat, RT & LT Objective transmission shroud
Objective (O)	LT-APO (Attocube)	Clear aperture 4.7 mm, f = 2.87 mm, working distance 0.65 mm, NA = 0.82, apochromatic range 465–590 nm
L2	LA4579-AB (ThorLabs)	f = 300 mm, 1″ diam., UVFS plano-convex lens, anti-reflection coated 400–1100 nm
L3	LA4148-AB (ThorLabs)	f = 50 mm or 100 mm, (see text), 1″ diam., UVFS plano-convex lens, anti-reflection coated 400–1100 nm
L4	LA4102-AB (ThorLabs)	f = 200 mm or 100 mm (see text), 1″ diam., UVFS plano-convex lens, anti-reflection coated 400–1100 nm
L5, L6	LA4936-AB (ThorLabs)	f = 30 mm, 0.5″ diam., UVFS plano-convex lens, anti-reflection coated 400–1100 nm
L7, L8	LA4647-AB (ThorLabs)	f = 20 mm, 0.5″ diam., UVFS plano-convex lens, anti-reflection coated 400–1100 nm
Spectrograph	Kymera 328i (Andor)	2 exit ports (to camera and intensity interferometer), 4-place turret with 1 mirror and 3 gratings, Solis software
Camera	ZL41 Wave 4.2 (Andor)	sCMOS camera, 4.2 megapixel sensor (6.5 μm pixel size) with 2048 × 2048 active pixels, 13.3 mm × 13.3 mm
Beam splitter (BS)	BSW10R (ThorLabs)	Non-polarizing, 50 : 50, 25 mm × 36 mm, 1 mm thick, UVFS, coating 400–700 nm
Single-photon avalanche diode (SPAD)	MPD-050-CTC (MPD/ PicoQuant)	50 μm active area, <100 dark counts, 27 ps jitter
Time-tagger (TT)	Time Tagger Ultra (Swabian Instruments)	4 channels, 8 ps time resolution (RMS jitter), 2.1 ns dead time

through a 4-meter-long optical fiber. From there, light propagated in free space. The choice of using a fiber over free space was motivated by space constraints (laser positioned away from the setup) and the desire to achieve a uniform beam profile at the sample. The spot size d_{L1} incident on the focusing lens L1 could be estimated using the specifications of the fiber coupler (outcoupling beam size and the divergence angle, under the assumption that the fiber is in the focus of the lens) and the distance between the fiber coupler and L1, or measured directly with a beam profiler or calibrated camera, if available.

One needs to ensure that the beam is collimated to use all the equations. However, in practice, it is not necessary. The result is judged by the size of the excitation spot at the sample. For the focusing lens L1, we chose a lens with a focal length of 125.4 mm, mounted on a flip holder approximately 9.5 bolt holes before the tip of the objective (Fig. 2, *ca.* 240 mm on a metric breadboard). The flip holder of L1 allows it to be retracted from the collimated beam so that the setup could be operated with a focused excitation beam. The collimated beam exiting the fiber coupler has a circular profile with a waist diameter of around 600 μm, as measured with a beam profiler (Fig. S2 in the SI). Using these values and the eqn (3), the calculated d_{spot} = 13.7 μm. The size of the excitation spot on the sample was quantified by imaging fluorescence from a uniform dried yellow highlighter ink film on a thin glass slide (Fig. 2d). Fitting the image with a 2D Gaussian yielded a nearly circular intensity distribution, with a spot size at the sample of 16.5 μm × 18 μm (waist diameter, Fig. S3), in reasonable agreement with the calculation. The scale bar calibration was performed with Nile red SPHERO™ Fluorescent Particles of mean diameter 2.11 ± 0.2 μm, which are shown in Fig. 2e. Error propagation led to a scalebar uncertainty of 11%. Upon close inspection of the image of the excitation spot (Fig. 2d), some structure in the intensity distribution can be observed. It is good to remember that due to the high coherence of the laser light, even minor imperfections in the optics and the presence of dust produce interference and diffraction-related structures in the excitation spot. The origin of that structure was attributed to the optics after the fiber, *i.e.*, the fiber coupler and L1, based on a visual inspection of the 405 nm beam projected onto paper. Without changing the objective, the size of d_{spot} can be changed by either changing d_{L1} (for example, by replacing a fiber coupler with an alternative configuration to collimate the output of the fiber) or f_{L1} (by replacing the lens). In either case, one needs to check that the beam enters the objective without clipping its clear aperture.

In the detection path, the light emitted by the sample is collected through the same objective, which serves as a collimating lens for PL (Fig. 1, 2b and c). The collimated PL is then focused with a tube lens L2 to form an image on the first image plane (IP1 at the f_{L2}). The magnification at IP1 is $M_{Obj+L2} = f_{L2}/f_{Obj}$ = 104.5. An iris diaphragm is placed at IP1 to select a region of interest from the entire image, as well as to

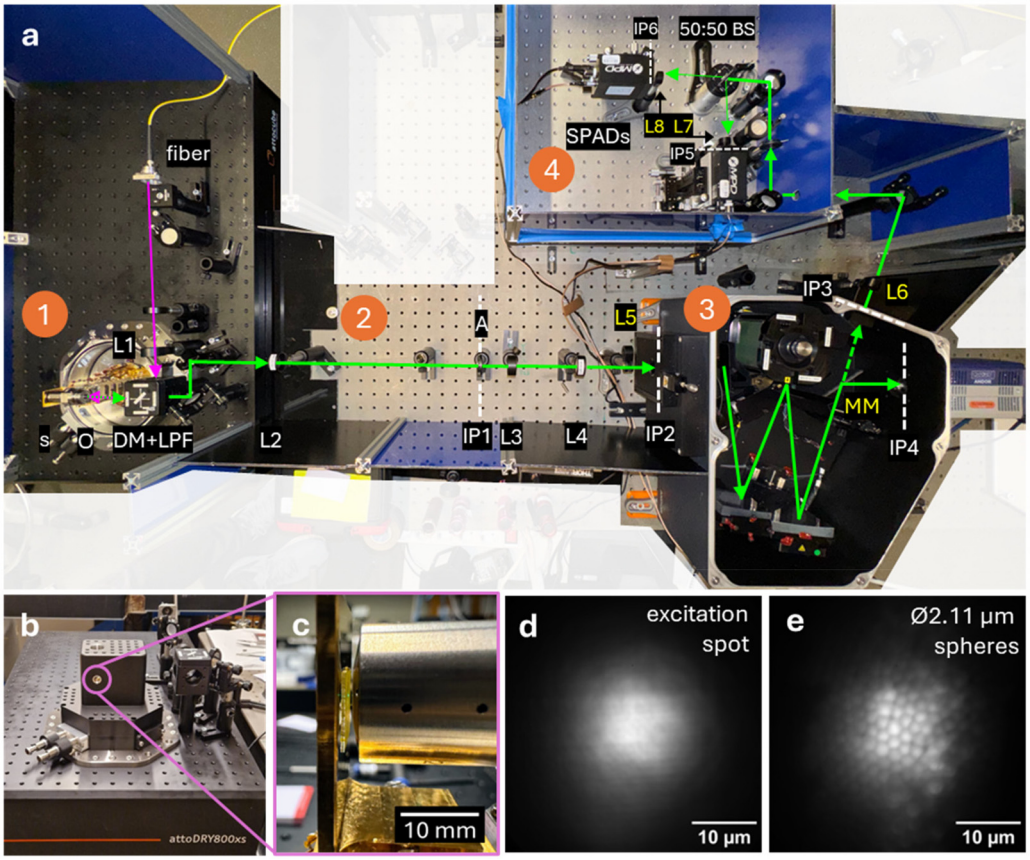

Fig. 2 (a) Photograph of the setup with overlay graphics highlighting the modules (1–4, as in Fig. 1), beam path, and optical elements (L5–L7 are specified in Table S1 in the SI). IP are image planes, MM is the moving mirror to select the exit port, IP1 – intermediate image plane, IP2 is the slip plane which is conjugated to IP3 (exit slit), IP4 – the camera chip plane, IP5 and IP6 are image planes at the SPADs. (b) Side view of the cryostat shroud enclosing the microscope objective, (c) the close-up photograph of the objective with 405 nm laser (not visible) exciting a green PL from a thin film sample, (d) excitation spot imaged as a PL of from a uniform film of dried yellow highlighter inks on a thin glass slide, (e) image of 2.11 µm SPHERO™ Fluorescent Particles used for length scale calibration.

provide a diagnostic for the correct focusing of the second image plane (IP2) on the camera. The light passing through the iris is then collected by a relay lens doublet (L3 and L4). L3 is a collimating lens placed at a distance f_{L3} from IP1, followed by the focusing lens L4 to obtain a further magnified image on IP2, an image plane at the entrance slit of the spectrograph. The magnification by relay lenses provides an additional factor of $M_{L3+L4} = f_{L4}/f_{L3}$, which was varied between 4× and 1×, depending on the choice of lenses (see Table 1), for a total magnification at IP2 of approximately 400× or 100×, respectively.

IP2 is imaged by the spectrograph with unity magnification on the plane of the exit slit as well as on the camera chip (IP4). Here, it is important to consider that the spatial resolution of the microscope is fundamentally limited by light diffraction and optical aberrations. So, depending on the camera pixel size, after a certain limit, increasing the magnification does not lead to an increase in resolution, but rather leads to useless spreading of the image over too many pixels. Due to this spread, the PL signal in each pixel goes down as the inverse square of the magnification. A compromise between having high resolution and a high number of counts per pixel (based on Nyquist criteria) is to have around 3 pixels per the full width of half maximum (FWHM) of the instrumental response function (IRF) of the microscope (the width of spatial distribution produced by a point source of light, *e.g.*, individual nanocrystal). Then the magnification in the IP4 plane is M = 3 × camera pixel size/$\mathrm{IRF}_{\mathrm{fwhm}}$. Diffraction-limited FWHM of IRF is approximately 0.61λ/NA or, in our case, ≈0.4 µm for NA = 0.82 and λ = 550 nm. Thus, the optimal magnification at the camera plane should be around M = 3 × 6.3 µm/0.4 µm ≈ 50×. It is important to note that there are theoretical considerations and practical implementations, each with its own limitations, and while they do not always coincide, understanding the theory remains essential.

To couple light into the HBT interferometer for photon statistics and PL lifetime measurements, we used lenses L5–L8. L5 was mounted on a flipping holder in front of the spectrograph entrance slit to focus the light and record the spectrum of the whole image (as further elaborated in the Performance section), so that when the spectrograph directed the beam toward the HBT interferometer, a focused output was delivered

onto L6. L6 collimated the beam, which then passed through a beamsplitter, while L7 and L8 refocused it onto the SPAD sensors with an estimated spot size 30–40 μm. It should also be noted that the SPAD pixel size must be equal to or larger than the diffraction limit, otherwise the signal is lost. Initial alignment of the beam through the spectrograph, beamsplitter, and SPADs was performed with a red HeNe laser. The SPADs were mounted on XYZ translation stages to allow fine alignment of the focused beam from the sample during measurements.

Several programming efforts supported the setup preparation. Before purchasing optical components (fiber, fiber coupler, lenses L1–L4), calculations were first carried out on paper and then verified by encoding the geometrical optics parameters in Python (v3.8.10 on Spyder v5.5.5); the script is available on GitHub.[31] During setup construction, we also used FRED Optimum and Winlens Basic to practice optical engineering and to verify ray tracing. Once the setup was completed and operational (see Performance section), the Andor spectrograph and Swabian time tagger were integrated into a single Python-based workflow to streamline data acquisition and processing.[32] This code, available in the SI, relies on manufacturer APIs and automates the sequential control of grating movement, initiation of TCSPC measurements, and data saving. All resulting data can be analyzed using in-house Python scripts (also available in the SI and on GitHub), which provide immediate graphical visualization, as demonstrated in the following section.

Performance

The setup was designed with microscopic luminescent samples in mind, such as perovskite nanocrystal superlattices.[27,29,33–37] Such superlattices, grown on flat substrates, have dimensions ranging from hundreds of nanometers up to tens of microns. To test the performance, we prepared samples of superlattices from colloidal 8 nm $CsPbBr_3$ nanocrystals, synthesized with oleic acid and oleylamine as capping ligands,[36] and treated with didodecyldimethylammonium bromide (DDAB) to boost PL and stability.[38]

As stated above, we used a 405 nm light source for the excitation. The 405 nm excitation is a common choice for lead halide perovskite such as $CsPbBr_3$, as it matches or falls above the absorption band edge across virtually an entire quantum-confinement range for this compound in the form of colloidal nanomaterial (from *ca.* 400 nm lowest excited state in <1 nm clusters,[39] to *ca.* 428 nm in 2-monolayer nanoplatelets,[40] 486 nm in *ca.* 5–6 nm nanocubes,[41] 502 nm in 7–8 nm nanocubes,[36] 508 nm for *ca.* 20 nm nanocubes,[42] and eventually to *ca.* 550 nm of the bulk $CsPbBr_3$ [43]).

With a *ca.* 20 μm excitation spot, the maximum excitation fluence at the sample was estimated to be 1 μJ cm^{-2} (losses include *ca.* 30% transmission of the incident laser power by the single-mode fiber), with the lower limit tunable down to *ca.* 0.01 μJ cm^{-2} by a combination of the laser's power settings and neutral density filters. The laser power loss arises primarily at the initial fiber-coupling step, and depends on the laser mode quality, the optical components, and the stability of the alignment. In the setup, the laser mode is not perfectly circular, which limits the coupling efficiency into a single-mode fiber. We used the single-mode fiber to improve the beam profile at the cost of power loss. If the beam profile is not critical, a multimode fiber could be employed to reduce these losses.

The 0.01–1 μJ cm^{-2} fluence range allows PL experiments on 8 nm $CsPbBr_3$ nanocubes with an excitation in the range of *ca.* 0.02–5 × 10^{-4} excitations per nanocrystal, using a size-dependent absorption cross-section of 8 × 10^{-15} cm^2 at 405 nm.[44] Compared with excitation conditions reported in the literature, the 0.01–1 μJ cm^{-2} range is suitable for studies of single-excitation superradiance[29,45–47] as well as routine PL imaging and spectroscopy. For studies of light emission at very high excitation intensities, *ca.* 10–10^5 μJ cm^{-2}, a regime reported in the studies of superfluorescence, the fluence can be increased by reducing d_{spot} (for example, focusing it by a factor of 3.3 will increase the excitation fluence by a factor of 10) or by using a more powerful laser source. It is worth keeping in mind that, for studies of superlattices sized at several microns, intense and tightly-focused d_{spot} below the dimensions of the superlattice may result in the highly non-uniform excitation of nanocrystals. One possibility to mitigate that could be the implementation of a flat top beam.[48]

Fig. 3 summarizes the steady-state μ-PL properties of a single *ca.* 6.7 × 7.3 μm superlattice at 5.6 K (the temperature at the top of the piezo-stack, near the sample) collected with the described setup at the excitation fluence of 0.3 μJ cm^{-2}. Fig. 3a and b shows μ-PL images of the superlattice at room and cryogenic temperatures, selected as a region of interest with an iris. Fig. 3b, c, e and f illustrates spectra from the region of interest as imaged on the camera and obtained from the lines 1 pixel wide corresponding to the location in the sample marked with coloured dots in Fig. 3a and d. This superlattice shows uniform PL spectra across the entire structure, both at room and cryogenic temperatures. The narrowing and shift of the PL spectra to longer wavelengths with decreasing temperature is typical for $CsPbBr_3$ semiconductor, both in bulk[49] and nanocrystals, and is not necessarily a signature of collective effects.[37]

The switching between imaging and spectral modes of the spectrograph was done by switching between a mirror and a grating (400 l mm^{-1}, blaze wavelength 550 nm) in the spectrograph. To collect PL spectra with a wavelength resolution it is necessary to close the spectrograph slits. This operation transforms the analyzed area of the image into a vertical line that is dispersed by the grating into its spectral components, enabling spectro-spatial correlation across the superlattice (in "spectral imaging mode"). To measure the spectrum from the entire image instead of the spatially resolved line, lens L5 was mounted on a flipping holder before the spectrograph (Fig. 2), allowing the sample image to be focused on the slit ("focused mode").

The collected data consists of .tif files for the PL sample images (Fig. 3a and d) and .asc files containing the spectral

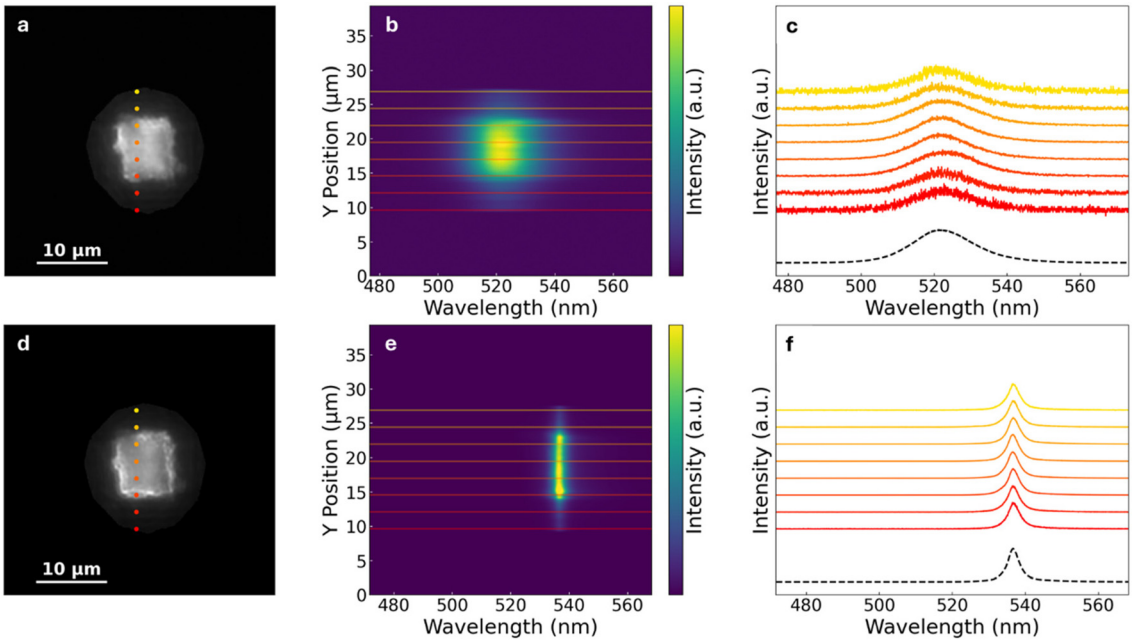

Fig. 3 Room- and cryogenic temperature µ-PL profiles of the superlattice self-assembled from $CsPbBr_3$ nanocrystals. (a and d) Images of the same perovskite nanocrystal superlattice at 294 K (room temperature) and 5.6 K. (b and e) Spectro-spatial correlation of the superlattice image along the vertical line marked by the coloured dots (spectral imaging mode, slit width 50 µm). (c and f) Position-specific PL spectra at positions on a superlattice marked with coloured dots together with a total spectrum of the superlattice acquired along the acquisition line (black dashed line).

information (Fig. 3b and e), including the metadata about the measurement conditions, as recorded by the spectrograph software. These files have been processed using a custom-written Python script to create a convenient spatio-spectral representation, *i.e.*, the entirety of Fig. 3. The data files and scripts are provided in the SI.

The capability to focus the image on the spectrograph slits is further necessary to collect spectrally resolved time-resolved PL measurements, as a spot that fits the detector's active area is required, as discussed earlier. As shown in Fig. 2, the HBT-interferometer for time-resolved PL and correlation measurements consists of two SPADs positioned at 90° to each other after a 50 : 50 beamsplitter placed at a 45° incident angle to the entering light beam. This detection configuration is commonly known as the Hanbury Brown and Twiss (HBT) interferometer.[50,51] It enables single photon detection and timing for time-correlated single photon counting (TCSPC), together with second-order correlation ($g^{(2)}$) measurements. The photons arrival signal generated by the SPADs is handled by a time-tagger (a fast electronic event counting device), allowing for a temporal instrument response function of the apparatus limited by the width of the laser pulse (approximately 200 ps). This configuration is compatible with further extensions such as the integration of Hong–Ou–Mandel (HOM) interferometry to study the indistinguishability of photons.[42,52] The optical path of the potential HOM interferometer is sketched in Fig. S4 in the SI. The performance of the TCSPC setup has been tested on a Rhodamine 6G solution in ethanol and a dilute film of $CsPbBr_3$ colloidal nanocrystals. The PL lifetime of Rhodamine was measured as 3.87 ns, in agreement with a reference value of 3.99 ns (Fig. S5).[53] An isolated emitter in the dilute film of weakly-confined $CsPbBr_3$ nanocrystals showed an expected spectrum and photon antibunching ($g^{(2)} \approx 0.4$, Fig. S6), verifying the functioning of the setup.

Fig. 4 shows the results of the cryogenic temperature measurement of the spectral dynamics of a sub-5 µm $CsPbBr_3$ nanocrystal superlattice, which exhibits multiple PL peaks (Fig. 4a and b) and was prepared from a different batch of nanocrystals than the superlattice discussed in Fig. 3. The setup enables recording of the PL intensity time decays over the entire spectral window (Fig. 4c) with decays for selected wavelengths across the spectrum are summarized in Fig. 4d. Fig. 4e and f shows the second-order correlation function of the different spectral components at the excitation fluence of 0.71 µJ cm^{-2}. The results show expected changes in the PL decay with the wavelength (*i.e.*, faster decay at 522 nm than at 530 nm due to the size-distribution and energy funnelling in superlattices),[37,54] and a constant $g^{(2)}(0)$ value of approximately 1 across the PL spectrum, as expected from the Poissonian statistic of light coming from an ensemble of emitters. This capability of the setup to resolve dynamics and correlation at different emitted wavelengths is fundamental to investigate collective phenomena such as superfluorescence and superradiance that are reportedly characterized as narrower, red-shifted, and accelerated PL compared to spontaneous emission, as well as with a bunched ($g^{(2)}(0) > 1$) photon statistics. The wavelength bandwidth of the measurements in Fig. 4c–f

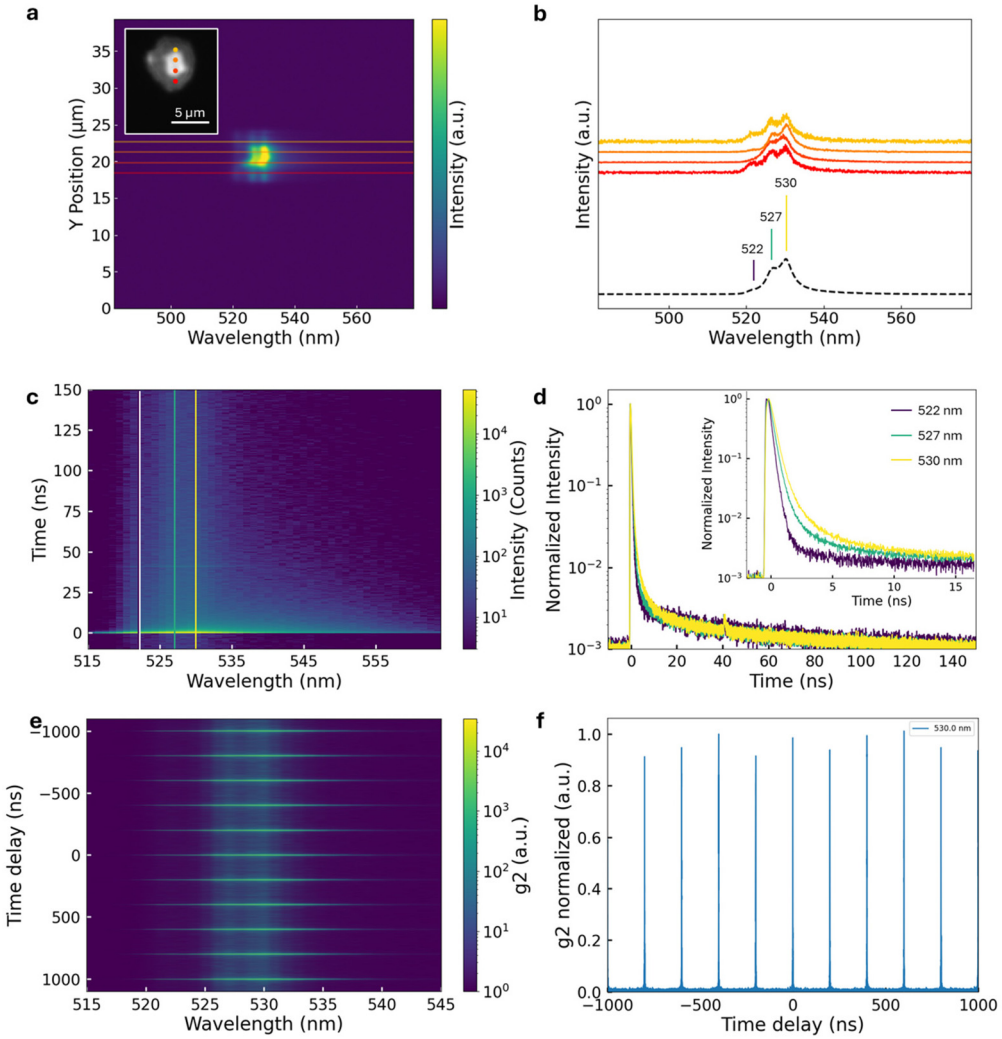

Fig. 4 Time-resolved PL and second-order photon correlation of a single superlattice at T = 5.6 K. (a and b) µ-PL profiles of a sub-5 µm $CsPbBr_3$ nanocrystal superlattice showing multiple PL peaks. (c and d) The time-resolved PL spectrum in the range 466–546 nm with a step size of 1 nm and extracted PL decays at three selected wavelengths (522, 527, and 530 nm, as marked with white, green, and yellow thin lines, respectively). (e and f) Spectrally-resolved second-order correlation measured at 530 nm.

can be tuned by adjusting the width of the output slit or the grating in the spectrograph, with the narrowest being 0.2 nm. As with the µ-PL measurement (Fig. 3), the data files and the script to analyze time-resolved PL data are provided in the SI.

Conclusions

In summary, we described the design and implementation of a cryo-optical setup for temperature-dependent wide-field PL microscopy and spectroscopy of luminescent nanomaterials. The setup features a wide-field PL microscope as a flexible basis, allowing extensions such as continuous-wave and pulsed excitation, polarization control, and configurations for imaging, steady-state, time-resolved spectroscopy, and photon correlation measurements. The setup performance is demonstrated on spectrally homogeneous and heterogeneous perovskite nanocrystal superlattices at room and cryogenic temperatures, showing its utility for investigations of emerging luminescent nanomaterials. The setup is universally applicable to luminescent materials and is not limited to perovskites. By offering a flexible and accessible platform, this work aims to lower the barrier to advanced PL characterization for chemists and materials scientists developing next-generation light-emitting materials for optoelectronic and quantum applications.

Author contributions

Lorenzo Tallarini: conceptualization (lead), data curation (equal), formal analysis (equal), funding acquisition (supporting), investigation (lead), methodology (lead), project administration (equal), resources (lead), software (equal), supervision (equal), validation (lead), visualization (equal), writing – orig-

inal draft preparation (lead), writing – review and editing (equal). **Gioele Lapo:** data curation (equal), formal analysis (equal), investigation (equal), methodology (supporting), software (equal), visualization (supporting). **Marzo López Cerón:** conceptualization (equal), data curation (equal), investigation (supporting), methodology (equal), resources (equal), software (lead), writing – review and editing (equal). **Ivan G. Scheblykin:** conceptualization (supporting), formal analysis (supporting), methodology (supporting), resources (supporting), supervision (supporting), validation (supporting), writing – review and editing (supporting). **Dmitry Baranov:** conceptualization (lead), data curation (supporting), formal analysis (supporting), funding acquisition (lead), investigation (supporting), methodology (equal), project administration (lead), resources (lead), software (supporting), supervision (lead), validation (supporting), visualization (supporting), writing – original draft preparation (lead), writing – review and editing (lead).

Conflicts of interest

There are no conflicts to declare.

Data availability

Data for this article, including raw data for Fig. 3 and 4, Python scripts for optical calculations, data processing, and integrating the Swabian time-tagger with the Andor spectrograph, are available in the supporting information (SI) and at Zenodo (https://doi.org/10.5281/zenodo.17216230).

Supplementary information: excitation spot characterization, complete list of the setup components, sketch of HOM setup, validation measurements of Rhodamine lifetime in solution and an isolated emitter in a sample of individual perovskite nanocrystals; original data and scripts. See DOI: https://doi.org/10.1039/d5nr04127a.

Acknowledgements

The work of LT, GL, MCL, and DB is funded by the European Union (ERC Starting Grant PROMETHEUS, project no. 101039683). Views and opinions expressed are, however, those of the authors only and do not necessarily reflect those of the European Union or the European Research Council Executive Agency. Neither the European Union nor the granting authority can be held responsible for them. LT and DB thank Lund Laser Center for financial support in acquiring SPADs. IS thanks the Swedish Research Council (project 2020-03530).

References

1 Z. Wei, M. Dubajic, C. Chosy, S. Kahmann and S. D. Stranks, *Nat. Rev. Methods Primers*, 2025, **5**, 37.
2 W. E. Moerner, *Rev. Mod. Phys.*, 2015, **87**, 1183–1212.
3 S. W. Hell, *Rev. Mod. Phys.*, 2015, **87**, 1169–1181.
4 E. Betzig, *Rev. Mod. Phys.*, 2015, **87**, 1153–1168.
5 R. Camacho, D. Täuber and I. G. Scheblykin, *Adv. Mater.*, 2019, **31**, 1805671.
6 D. Wöll and C. Flors, *Small Methods*, 2017, **1**, 1700191.
7 A. Merdasa, Y. Tian, R. Camacho, A. Dobrovolsky, E. Debroye, E. L. Unger, J. Hofkens, V. Sundström and I. G. Scheblykin, *ACS Nano*, 2017, **11**, 5391–5404.
8 A. Naumov, I. Y. Eremchev and A. A. Gorshelev, *Eur. Phys. J. D*, 2014, **68**, 348.
9 B. Louis, S. Seth, Q. An, R. Ji, Y. Vaynzof, J. Hofkens and I. G. Scheblykin, *Adv. Mater.*, 2025, **37**, 2413126.
10 M. Gerhard, B. Louis, R. Camacho, A. Merdasa, J. Li, A. Kiligaridis, A. Dobrovolsky, J. Hofkens and I. G. Scheblykin, *Nat. Commun.*, 2019, **10**, 1698.
11 A. Merdasa, M. Bag, Y. Tian, E. Källman, A. Dobrovolsky and I. G. Scheblykin, *J. Phys. Chem. C*, 2016, **120**, 10711–10719.
12 I. Y. Eremchev, A. O. Tarasevich, M. A. Kniazeva, J. Li, A. V. Naumov and I. G. Scheblykin, *Nano Lett.*, 2023, **23**, 2087–2093.
13 J. Almutlaq, Y. Liu, W. J. Mir, R. P. Sabatini, D. Englund, O. M. Bakr and E. H. Sargent, *Nat. Nanotechnol.*, 2024, **19**, 1091–1100.
14 C. R. Kagan, L. C. Bassett, C. B. Murray and S. M. Thompson, *Chem. Rev.*, 2020, **121**, 3186–3233.
15 H. A. Nguyen, G. Dixon, F. Y. Dou, S. Gallagher, S. Gibbs, D. M. Ladd, E. Marino, J. C. Ondry, J. P. Shanahan, E. S. Vasileiadou, S. Barlow, D. R. Gamelin, D. S. Ginger, D. M. Jonas, M. G. Kanatzidis, S. R. Marder, D. Morton, C. B. Murray, J. S. Owen, D. V. Talapin, M. F. Toney and B. M. Cossairt, *Chem. Rev.*, 2023, **123**, 7890–7952.
16 C. Tsao, H. Ling, A. Hinkle, Y. Chen, K. K. Jha, Z.-L. Yan and H. Utzat, *Nat. Nanotechnol.*, 2025, **20**, 1001–1016.
17 J. Zhu, Y. Li, X. Lin, Y. Han and K. Wu, *Nat. Mater.*, 2024, **23**, 1027–1040.
18 B. Russ and C. N. Eisler, *Nanophotonics*, 2024, **13**, 1943–1951.
19 Y. Tang, Y. Jing, T. C. Sum, A. Bruno and S. G. Mhaisalkar, *Adv. Energy Mater.*, 2025, **15**, 2400322.
20 F. Hu, C. Yin, H. Zhang, C. Sun, W. W. Yu, C. Zhang, X. Wang, Y. Zhang and M. Xiao, *Nano Lett.*, 2016, **16**, 6425–6430.
21 G. Rainò, G. Nedelcu, L. Protesescu, M. I. Bodnarchuk, M. V. Kovalenko, R. F. Mahrt and T. Stöferle, *ACS Nano*, 2016, **10**, 2485–2490.
22 M. Fu, P. Tamarat, H. Huang, J. Even, A. L. Rogach and B. Lounis, *Nano Lett.*, 2017, **17**, 2895–2901.
23 B. Li, H. Huang, G. Zhang, C. Yang, W. Guo, R. Chen, C. Qin, Y. Gao, V. P. Biju, A. L. Rogach, L. Xiao and S. Jia, *J. Phys. Chem. Lett.*, 2018, **9**, 6934–6940.
24 Y. Lv, C. Yin, C. Zhang, W. W. Yu, X. Wang, Y. Zhang and M. Xiao, *Nano Lett.*, 2019, **19**, 4442–4447.
25 J. Liu, C. Zhu, M. Pols, Z. Zhang, F. Hu, L. Wang, C. Zhang, Z. Liu, S. Tao, M. Xiao and X. Wang, *Nano Lett.*, 2023, **23**, 10089–10096.

26 Z. Liu, X. Qin, Q. Chen, T. Jiang, Q. Chen and X. Liu, *Adv. Mater.*, 2023, **35**, e2209279.
27 G. Raino, M. A. Becker, M. I. Bodnarchuk, R. F. Mahrt, M. V. Kovalenko and T. Stoferle, *Nature*, 2018, **563**, 671–675.
28 D. D. Blach, V. A. Lumsargis-Roth, C. Chuang, D. E. Clark, S. Deng, O. F. Williams, C. W. Li, J. Cao and L. Huang, *Nat. Commun.*, 2025, **16**, 1270.
29 D. D. Blach, V. A. Lumsargis, D. E. Clark, C. Chuang, K. Wang, L. Dou, R. D. Schaller, J. Cao, C. W. Li and L. Huang, *Nano Lett.*, 2022, **22**, 7811–7818.
30 E. Hecht, *Optics*, Pearson Education India, 2012.
31 M. López Cerón, 2024. https://github.com/marzo-lc/Optical-Path-Design-for-a-Cryo-Optical-Photoluminescence-Microscopy-Setup.
32 Y. Xie, K. He and A. Castellanos-Gomez, *Small Struct.*, 2025, **6**, 2500173.
33 Y. Nagaoka, K. Hills-Kimball, R. Tan, R. Li, Z. Wang and O. Chen, *Adv. Mater.*, 2017, **29**, 1606666.
34 Y. Tong, E.-P. Yao, A. Manzi, E. Bladt, K. Wang, M. Döblinger, S. Bals, P. Müller-Buschbaum, A. S. Urban, L. Polavarapu and J. Feldmann, *Adv. Mater.*, 2018, **30**, 1801117.
35 J. S. van der Burgt, J. J. Geuchies, B. van der Meer, H. Vanrompay, D. Zanaga, Y. Zhang, W. Albrecht, A. V. Petukhov, L. Filion, S. Bals, I. Swart and D. Vanmaekelbergh, *J. Phys. Chem. C*, 2018, **122**, 15706–15712.
36 D. Baranov, S. Toso, M. Imran and L. Manna, *J. Phys. Chem. Lett.*, 2019, **10**, 655–660.
37 D. Baranov, A. Fieramosca, R. X. Yang, L. Polimeno, G. Lerario, S. Toso, C. Giansante, M. Giorgi, L. Z. Tan, D. Sanvitto and L. Manna, *ACS Nano*, 2021, **15**, 650–664.
38 M. Imran, P. Ijaz, L. Goldoni, D. Maggioni, U. Petralanda, M. Prato, G. Almeida, I. Infante and L. Manna, *ACS Energy Lett.*, 2019, **4**, 819–824.
39 L. Peng, A. Dutta, R. Xie, W. Yang and N. Pradhan, *ACS Energy Lett.*, 2018, **3**, 2014–2020.
40 S. Toso, D. Baranov, C. Giannini and L. Manna, *ACS Nano*, 2021, **15**, 20341–20352.
41 M. Gomes Ferreira, B. Gastin, J. Hiller, I. A. Zaluzhnyy, G. N. Hinsley, B. Wang, K. H. Ngoi, I. A. Vartanyants, F. Schreiber, M. Scheele and D. Baranov, *Small Struct.*, 2025, **6**, 2500133.
42 A. E. K. Kaplan, C. J. Krajewska, A. H. Proppe, W. Sun, T. Sverko, D. B. Berkinsky, H. Utzat and M. G. Bawendi, *Nat. Photonics*, 2023, **17**, 775–780.
43 C. C. Stoumpos, C. D. Malliakas, J. A. Peters, Z. Liu, M. Sebastian, J. Im, T. C. Chasapis, A. C. Wibowo, D. Y. Chung, A. J. Freeman, B. W. Wessels and M. G. Kanatzidis, *Cryst. Growth Des.*, 2013, **13**, 2722–2727.
44 N. S. Makarov, S. Guo, O. Isaienko, W. Liu, I. Robel and V. I. Klimov, *Nano Lett.*, 2016, **16**, 2349–2362.
45 H. Pashaei Adl, S. Gorji, G. Muñoz–Matutano, A. F. Gualdrón–Reyes, I. Suárez, V. S. Chirvony, I. Mora–Seró and J. P. Martínez–Pastor, *Adv. Opt. Mater.*, 2023, **11**, 2202497.
46 S. Levy, O. Be'er, S. Shaek, A. Gorlach, E. Scharf, Y. Ossia, R. Liran, K. Cohen, R. Strassberg, I. Kaminer, U. Banin and Y. Bekenstein, *ACS Nano*, 2025, **19**, 963–971.
47 L. Luo, X. Tang, J. Park, C.-W. Wang, M. Park, M. Khurana, A. Singh, J. Cheon, A. Belyanin, A. V. Sokolov and D. H. Son, *Nano Lett.*, 2025, **25**, 6176–6183.
48 A. Laskin, P. Kaiser, V. Laskin and A. Ostrun, *Proc. SPIE – Photonic Solutions for Better Health Care V*, 2016, **9887**, 98872E1–10.
49 Y. Guo, O. Yaffe, T. D. Hull, J. S. Owen, D. R. Reichman and L. E. Brus, *Nat. Commun.*, 2019, **10**, 1175.
50 R. H. Brown and R. Q. Twiss, *Philos. Mag.*, 1954, **45**, 663–682.
51 H. J. Kimble, M. Dagenais and L. Mandel, *Phys. Rev. Lett.*, 1977, **39**, 691–695.
52 C. K. Hong, Z. Y. Ou and L. Mandel, *Phys. Rev. Lett.*, 1987, **59**, 2044–2046.
53 D. Magde, R. Wong and P. G. Seybold, *Photochem. Photobiol.*, 2002, **75**, 327–334.
54 S. A. Crooker, J. A. Hollingsworth, S. Tretiak and V. I. Klimov, *Phys. Rev. Lett.*, 2002, **89**, 186802.